Comparison between kinetic and fluid simulations of slab ion temperature gradient driven turbulence

H. Sugama and T.-H. Watanabe
National Institute for Fusion Science/Graduate University for Advanced Studies, Toki 509-5292, Japan

W. Horton
Institute for Fusion Studies, The University of Texas at Austin, Austin, Texas 78712

(Received 3 September 2002; accepted 16 December 2002)

A detailed comparison between kinetic and fluid simulations of collisionless slab ion temperature gradient driven turbulence is made. The nondissipative closure model (NCM) for linearly unstable modes, which is presented by Sugama, Watanabe, and Horton [Phys. Plasmas **8**, 2617 (2001)], and the dissipative closure model by Hammett and Perkins (HP) [Phys. Rev. Lett. **64**, 3019 (1990)] are used in separate fluid simulations. The validity of these closure models for quantitative prediction of the turbulent thermal transport is examined by comparing nonlinear results of the fluid simulations with those of the collisionless kinetic simulation of high accuracy. Simulation results show that, in the saturated turbulent state, the turbulent thermal diffusivity χ obtained from the HP model is significantly larger than the χ given by the NCM which is closer to χ measured in the kinetic simulation. Contrary to the dissipative form of the parallel heat flux closure relation assumed in the HP model, the NCM describes well the exact kinetic simulation, in which for some unstable wave numbers $\mathbf{k}$, the imaginary part of the ratio of the parallel heat flux $q_{\mathbf{k}}$ to the temperature fluctuation $T_{\mathbf{k}}$ is a oscillatory function of time and sometimes takes positive values. The positive values of $\mathrm{Im}(q_{\mathbf{k}}/T_{\mathbf{k}})$, imply the negative parallel heat diffusivity, correlate with the occasional inward heat flux occurring for the wave numbers $\mathbf{k}$, and reduce the total χ. © *2003 American Institute of Physics.* [DOI: 10.1063/1.1544664]

I. INTRODUCTION

In recent years, gyrokinetic and gyrofluid (or gyro-Landau-fluid) simulations[1] of plasma turbulence driven by microinstabilities such as the ion temperature gradient (ITG) mode,[2] have actively been done in order to predict the anomalous transport coefficients in magnetically confined plasmas from the first principle. Since the gyrofluid simulations[3–5] consume less computer memory and time than the gyrokinetic simulations,[6–9] the former is useful for doing many runs to establish the scaling model of the anomalous transport coefficients. However, in the gyrofluid model, some closure relations[10–12] are assumed to construct a truncated system of fluid equations from the gyrokinetic equation and their validity in nonlinear or turbulent regimes is not clear because conventional gyrofluid closure models, such as the Hammett–Perkins (HP) model,[10] were originally derived so as to accurately reproduce gyrokinetic dispersion relations for linear modes. In fact, there exist some cases, in which the gyrokinetic and gyrofluid simulations show disagreements in their nonlinear results, such as the saturated fluctuation levels and the turbulent transport coefficients.[1,13]

In our previous work,[14] we have presented the nondissipative closure model (NCM), which takes into account the time reversal symmetry of the collisionless kinetic equation. The NCM relates the parallel heat flux to the temperature and the parallel flow in terms of the real-valued coefficients in the unstable wave number space. The NCM was derived such that the closure relation is valid both for the unstable normal-mode solution and its complex-conjugate solution as well as for any linear combination of these solutions. Thus, in the NCM, the phase of the parallel heat flux with respect to the temperature fluctuation in the unstable wave number region can take either of positive and negative signs in the turbulent states while it takes only the one-sided sign in dissipative closure models such as the HP model. These different closure schemes lead to different nonlinear behaviors of the fluid variables even though they give almost the same linear results. In fact, a fluid system of equations using the NCM theory for unstable modes reproduces the exact nonlinear kinetic solution of the three-mode ITG problem[6,12,14] found by Watanabe, Sugama, and Sato[15] while the HP model fails in representing that solution. Then, the next question is whether the NCM can successfully describe strongly turbulent states of collisionless kinetic systems with a higher number of degrees of freedom. In the present work, in order to answer this question, we do both fluid and kinetic simulations of the two-dimensional slab ITG turbulence and investigate how accurately the fluid simulation using the NCM or the HP model can reproduce results of the collisionless kinetic simulation under the same conditions.

Zonal flows have been attracting much theoretical and experimental attention as one of important factors affecting the turbulence saturation level and the anomalous transport.[16] A wrong description of zonal flow damping in the original gyrofluid model was once suspected as a cause of difference between the gyrokinetic and gyrofluid simulation results.[17] Subsequently, the gyrofluid model was improved to correctly treat the zonal flow damping.[18] However, our work shows

that the closure relations for the fluctuations other than the zonal flow component are important, as well, because the gyrokinetic and gyrofluid simulations can show significant disagreements even for no zonal flow case. In this paper, we consider the no-flow case to examine the pure effects of the closure relations on the turbulence saturation. Adding the complexity caused by the feedback–feedforward coupling of zonal flows obscures the role of the closure problem for the fluctuations. Simulation results with flows included are not shown here also because only quiet steady states with turbulence transport suppressed are obtained by both of our gyrokinetic and gyrofluid simulations of the two-dimensional slab ITG turbulence when the zonal flow component is included.[19] In toroidal configurations, such effects as the collisionless transit time magnetic pumping and the neoclassical viscosity would cause stronger damping of the zonal flow[20] and accordingly larger turbulence transport than in the two-dimensional case.

The rest of this work is organized as follows: In Sec. II, the basic kinetic and fluid equations for simulating the collisionless slab ITG turbulence are presented. There, a detailed expression of the NCM used for the parallel heat flux in the temperature evolution equation is given. Also, the kinetic and fluid entropy balance equations are derived from those basic equations in order to describe the quasisteady turbulence state in which the entropy variable associated with fine velocity-space structures monotonically grows but the low-order-moment fluid variables' fluctuations and the turbulent transport are saturated. In Sec. III, results of the kinetic and fluid simulations of the two-dimensional slab ITG turbulence are shown. Two different types of fluid simulations are done to separately examine the validity of the NCM and HP closure models compared with the kinetic simulation results. The quasisteady state is realized by the kinetic simulation with no zonal flow component. The saturated fluctuation level, the turbulent heat diffusivity, and the ratio of the parallel heat flux to the temperature fluctuation obtained by the fluid simulations are directly compared with those in the kinetic simulation, and effects of the closure models on the resultant transport are specified. Finally, conclusions are given in Sec. IV.

II. BASIC EQUATIONS

The collisionless electrostatic gyrokinetic equation for ions in the uniform magnetic field $\mathbf{B}$ is written as[21]

$$\frac{\partial f}{\partial t}+\left(v_{\parallel}\mathbf{b}+\frac{c}{B}\mathbf{b}\times\nabla\langle\phi(\mathbf{x}+\boldsymbol{\rho})\rangle\right)\cdot\nabla f - \frac{e}{m_i}\mathbf{b}\cdot\nabla\langle\phi(\mathbf{x}+\boldsymbol{\rho})\rangle\frac{\partial f}{\partial v_{\parallel}}=0, \tag{1}$$

where $f=f(\mathbf{x},v_{\parallel},\mu,t)$ represents the ion gyrocenter distribution function, $\mathbf{x}$ is the ion gyrocenter position, $v_{\parallel}$ is the velocity component parallel to $\mathbf{B}$, $\mu\equiv m_i v_{\perp}^2/2B$ is the magnetic moment, and $\langle\phi(\mathbf{x}+\boldsymbol{\rho})\rangle$ is the electrostatic potential averaged with respect to the gyrophase included in the ion gyroradius vector $\boldsymbol{\rho}$. Here, $\boldsymbol{\rho}$ is defined by $\boldsymbol{\rho}\equiv\mathbf{b}\times\mathbf{v}_{\perp}/\Omega_i$ with the perpendicular velocity $\mathbf{v}_{\perp}$, the ion gyrofrequency $\Omega_i\equiv eB/(m_i c)$, and the unit vector $\mathbf{b}$ parallel to $\mathbf{B}$.

The distribution function f is given by the sum of a background Maxwellian part $f_M=n_0(m_i/2\pi T_i)^{3/2}\times\exp(-m_i v^2/2T_i)$ and a perturbation part $\tilde{f}$, where n_0 and T_i denote the background density and temperature, respectively, which macroscopically depend on a coordinate x in the perpendicular direction. Furthermore, in order to make numerical simulation easy, we assume $v_{\perp}$-dependence of $\tilde{f}$ to be also given in the Maxwellian form. Then, the fluctuation quantities $\tilde{f}$ and ϕ are written in terms of the Fourier expansion as

$$\tilde{f}(\mathbf{x},v_{\parallel},\mu,t)=\frac{m_i}{2\pi T_i}\exp\left(-\frac{m_i v_{\perp}^2}{2T_i}\right)\sum_{\mathbf{k}} f_{\mathbf{k}}(v_{\parallel},t)e^{i\mathbf{k}\cdot\mathbf{x}},$$
$$\phi(\mathbf{x},t)=\sum_{\mathbf{k}}\phi_{\mathbf{k}}(t)e^{i\mathbf{k}\cdot\mathbf{x}}, \tag{2}$$

where macroscopic variations of n_0 and T_i in the x-direction are considered separately from microscopic spatial variations represented by the wave number vector $\mathbf{k}$. Substituting Eq. (2) into Eq. (1) and integrating over $\mathbf{v}_{\perp}$-space, we obtain

$$\partial_t f_{\mathbf{k}}+ik_{\parallel}v_{\parallel}f_{\mathbf{k}}-\frac{c}{B}\sum_{\mathbf{k}'+\mathbf{k}''=\mathbf{k}}[\mathbf{b}\cdot(\mathbf{k}'\times\mathbf{k}'')]\Psi_{\mathbf{k}'}f_{\mathbf{k}''} =i\left[\omega_{*i}\left\{1+\eta_i\left(\frac{m_i v_{\parallel}^2}{2T_i}-\frac{1}{2}-\frac{1}{2}b_{\mathbf{k}}\right)\right\}-k_{\parallel}v_{\parallel}\right]F_M\frac{e\Psi_{\mathbf{k}}}{T_i}, \tag{3}$$

where $k_{\parallel}\equiv\mathbf{k}\cdot\mathbf{b}$ is the parallel wave number, $\Psi_{\mathbf{k}}\equiv\phi_{\mathbf{k}}\exp(-b_{\mathbf{k}}/2)$ is the wave-number-space representation of the electrostatic potential averaged with respect to the gyrophase and $v_{\perp}$, $b_{\mathbf{k}}\equiv k_{\perp}^2T_i/(m_i\Omega_i^2)$ is the square of the perpendicular wave number multiplied by the thermal gyroradius, and $F_M\equiv\int d^2v_{\perp}f_M=n_0(m_i/2\pi T_i)^{1/2}\exp(-m_i v_{\parallel}^2/2T_i)$. Here, the parallel nonlinearity $-(e/m_i)\mathbf{b}\cdot\nabla\langle\phi(\mathbf{x}+\boldsymbol{\rho})\rangle\partial\tilde{f}/\partial v_{\parallel}$ included in Eq. (1) is neglected based on the gyrokinetic ordering $k_{\parallel}/k_{\perp}\sim k_{\parallel}\rho\ll 1$, and inhomogeneities in n_0 and T_0 are taken into account only through $\omega_{*i}\equiv(cT_i/eB)\mathbf{b}\cdot\mathbf{b}\times\nabla\ln n_0$ and $\eta_i\equiv d\ln T_i/d\ln n_0$ while n_0 and T_i in other places as well as ω_{*i} and η_i are regarded as constants.

Taking the velocity moments of Eq. (3), we obtain fluid equations,

$$\partial_t n_{\mathbf{k}}+ik_{\parallel}n_0u_{\mathbf{k}}-i\omega_{*i}n_0\left(1-\frac{b_{\mathbf{k}}}{2}\eta_i\right)\frac{e\Psi_{\mathbf{k}}}{T_i} -\frac{c}{B}\sum_{\mathbf{k}'+\mathbf{k}''=\mathbf{k}}[\mathbf{b}\cdot(\mathbf{k}'\times\mathbf{k}'')]\Psi_{\mathbf{k}'}n_{\mathbf{k}''}=0, \tag{4}$$

$$n_0m_i\partial_t u_{\mathbf{k}}+ik_{\parallel}(T_in_{\mathbf{k}}+n_0T_{\mathbf{k}}+n_0e\Psi_{\mathbf{k}}) -\frac{n_0m_ic}{B}\sum_{\mathbf{k}'+\mathbf{k}''=\mathbf{k}}[\mathbf{b}\cdot(\mathbf{k}'\times\mathbf{k}'')]\Psi_{\mathbf{k}'}u_{\mathbf{k}''}=0, \tag{5}$$

$$n_0\partial_t T_{\mathbf{k}}+ik_{\parallel}(2n_0T_iu_{\mathbf{k}}+q_{\mathbf{k}})-i\omega_{*i}\eta_in_0e\Psi_{\mathbf{k}} -\frac{n_0c}{B}\sum_{\mathbf{k}'+\mathbf{k}''=\mathbf{k}}[\mathbf{b}\cdot(\mathbf{k}'\times\mathbf{k}'')]\Psi_{\mathbf{k}'}T_{\mathbf{k}''}=0, \tag{6}$$

where $n_{\mathbf{k}}(t)\equiv\int_{-\infty}^{\infty}dv_{\parallel}f_{\mathbf{k}}(v_{\parallel},t)$, $n_0u_{\mathbf{k}}(t)\equiv\int_{-\infty}^{\infty}dv_{\parallel}\times f_{\mathbf{k}}(v_{\parallel},t)v_{\parallel}$, $n_0T_{\mathbf{k}}(t)\equiv\int_{-\infty}^{\infty}dv_{\parallel}f_{\mathbf{k}}(v_{\parallel},t)(m_iv_{\parallel}^2-T_i)$, and $q_{\mathbf{k}}(t)\equiv\int_{-\infty}^{\infty}dv_{\parallel}f_{\mathbf{k}}(v_{\parallel},t)(m_iv_{\parallel}^3-3T_iv_{\parallel})$. Here all nonlinear terms result from the $\mathbf{E}\times\mathbf{B}$ drift.

Assuming the adiabatic electron response and using the quasineutrality condition give

$$\exp(-b_{\mathbf{k}}/2)n_{\mathbf{k}}-n_0\frac{e\phi_{\mathbf{k}}}{T_i}[1-\Gamma_0(b_{\mathbf{k}})]=\frac{e\phi_{\mathbf{k}}}{T_e}\quad(\text{for } k_{\parallel}\neq0),\tag{7}$$

where Γ_0 is defined by $\Gamma_0(b_{\mathbf{k}})\equiv I_0(b_{\mathbf{k}})\exp(-b_{\mathbf{k}})$ with the zeroth-order modified Bessel function I_0. Here, the left and right-hand sides represent the ion and electron particle density fluctuations, respectively. In the left-hand side of Eq. (7), the ion gyrocenter density $n_{\mathbf{k}}$ is multiplied by the factor $\exp(-b_{\mathbf{k}}/2)$ due to the finite-Larmor-radius (FLR) effect and the second term with the electrostatic potential $\phi_{\mathbf{k}}$ results from the ion polarization. Dorland and Hammett[3] employed $[\Gamma_0(b_{\mathbf{k}})]^{1/2}$ instead of $\exp(-b_{\mathbf{k}}/2)$ for the FLR factor included in Eq. (7) and in $\Psi_{\mathbf{k}}$, which gives the same linear dispersion relation as that obtained by a rigorous treatment of $\mathbf{v}_{\perp}$-dependence of $\tilde{f}$. The difference between $\exp(-b_{\mathbf{k}}/2)$ and $[\Gamma_0(b_{\mathbf{k}})]^{1/2}$ is small for $b_{\mathbf{k}}<1$. For the purpose of comparison between nonlinear results of the kinetic and fluid simulations under the same conditions, it is not essential which FLR factor is used.

For the fluctuations with $k_{\parallel}=0$, the electron density perturbation is often assumed to vanish and then the quasineutrality condition gives

$$\exp(-b_{\mathbf{k}}/2)n_{\mathbf{k}}-n_0\frac{e\phi_{\mathbf{k}}}{T_i}[1-\Gamma_0(b_{\mathbf{k}})]=0\quad(\text{for } k_{\parallel}=0).\tag{8}$$

When using Eqs. (3), (7), and (8) for the two-dimensional slab ITG turbulence simulation, we have found that a large zonal flow component, $\phi_{\mathbf{k}}$ with $k_{\parallel}=0$, is nonlinearly generated, suppresses linearly-unstable modes with $k_{\parallel}\neq0$, and results in no turbulent transport.[19] Thus, efficiency of zonal flow generation and resultant transport coefficients are strongly influenced by what condition is used for the $k_{\parallel}=0$ modes. In more practical cases of toroidal configurations, the zonal flow would be significantly reduced by the collisionless transit time magnetic pumping and by the collisional damping[20] although neither of these effects is included in Eqs. (1) and (3). Here, in order to avoid the complexity brought about by the zonal flow and get finite turbulent transport, we put

$$f_{\mathbf{k}}=\phi_{\mathbf{k}}=0\quad(\text{for } k_{\parallel}=0),\tag{9}$$

and

$$n_{\mathbf{k}}=u_{\mathbf{k}}=T_{\mathbf{k}}=\phi_{\mathbf{k}}=0\quad(\text{for } k_{\parallel}=0),\tag{10}$$

in our kinetic and fluid simulations, respectively.

Now, a closed nonlinear kinetic system of equations are given by Eqs. (3) and (7) for $k_{\parallel}\neq0$ and by Eq. (9) for $k_{\parallel}=0$, which are used for kinetic simulation of the slab ITG turbulence in the present work. In order to obtain a corresponding closed fluid system, we need to express the parallel heat flow $q_{\mathbf{k}}$ in Eq. (6) in terms of the lower-order moment fluid variables $n_{\mathbf{k}}$, $u_{\mathbf{k}}$, and $T_{\mathbf{k}}$. In the HP model,[10] $q_{\mathbf{k}}$ is written in the diffusive form as

$$q_{\mathbf{k}}=-n_0\chi_{\parallel}ik_{\parallel}T_{\mathbf{k}},\tag{11}$$

where the parallel heat diffusivity is given by $\chi_{\parallel}=2(2/\pi)^{1/2}v_t/|k_{\parallel}|$ with the ion thermal velocity $v_t\equiv(T_i/m_i)^{1/2}$. Then, Eqs. (4)–(7) for $k_{\parallel}\neq0$, Eq. (10) for $k_{\parallel}=0$, and Eq. (11) give a closed fluid system of equations in the HP model. In the NCM, the parallel heat flow $q_{\mathbf{k}}$ in the unstable wave number region is given as[14]

$$q_{\mathbf{k}}=C_{T\mathbf{k}}n_0v_tT_{\mathbf{k}}+C_{u\mathbf{k}}n_0T_iu_{\mathbf{k}}\quad(\text{for linearly unstable modes}),\tag{12}$$

while the dissipative closure relation as written in Eq. (11) should still be used in the stable wave number region. Requiring that the closure relation in Eq. (12) should exactly reproduce the kinetic dispersion relation, the real-valued coefficients $C_{T\mathbf{k}}$ and $C_{u\mathbf{k}}$ are determined as

$$C_{T\mathbf{k}}=C_{Lr\mathbf{k}}-C_{Li\mathbf{k}}\frac{\mathrm{Re}(\xi_{\mathbf{k}}\zeta_{\mathbf{k}}^*)}{\mathrm{Im}(\xi_{\mathbf{k}}\zeta_{\mathbf{k}}^*)},$$

$$C_{u\mathbf{k}}=C_{Li\mathbf{k}}\frac{|\zeta_{\mathbf{k}}|^2}{\mathrm{Im}(\xi_{\mathbf{k}}\zeta_{\mathbf{k}}^*)},\tag{13}$$

where $C_{L\mathbf{k}}\equiv C_{Lr\mathbf{k}}+iC_{Li\mathbf{k}}\equiv-Z^{(3)}(\omega_{L\mathbf{k}}/(\sqrt{2}k_{\parallel}v_t))/[\sqrt{2}Z^{(2)}\times(\omega_{L\mathbf{k}}/(\sqrt{2}k_{\parallel}v_t))]$ [$Z^{(n)}$: is the nth derivative of the plasma dispersion function], $\xi_{\mathbf{k}}\equiv\xi_{r\mathbf{k}}+i\xi_{i\mathbf{k}}\equiv[\omega_{L\mathbf{k}}\{1+(T_e/T_i)(1-\Gamma_0(b_{\mathbf{k}}))\}-\omega_{*e}(1-b_{\mathbf{k}}\eta_i/2)e^{-b_{\mathbf{k}}}]/(k_{\parallel}v_t)$, and $\zeta_{\mathbf{k}}\equiv\zeta_{r\mathbf{k}}+i\zeta_{i\mathbf{k}}\equiv\omega_{L\mathbf{k}}\xi_{\mathbf{k}}/(k_{\parallel}v_t)-1-(T_e/T_i)(1-\Gamma_0(b_{\mathbf{k}})+e^{-b_{\mathbf{k}}})$ are used. The complex-valued eigenfrequency, $\omega_{L\mathbf{k}}$ is determined by the dispersion relation $D_{\mathbf{k}}(\omega_{L\mathbf{k}})=0$, where the dispersion function $D_{\mathbf{k}}(\omega)$ is defined by

$$D_{\mathbf{k}}(\omega)\equiv1-\Gamma_0(b_{\mathbf{k}})+e^{-b_{\mathbf{k}}}+\frac{T_i}{T_e}-e^{-b_{\mathbf{k}}}\int dv_{\parallel}\frac{e^{-v_{\parallel}^2/(2v_t^2)}}{\sqrt{2\pi}v_t}\times\frac{\omega-\omega_{*i}[1+\eta_i\{v_{\parallel}^2/(2v_t^2)-1/2-b_{\mathbf{k}}/2\}]}{\omega-k_{\parallel}v_{\parallel}}.\tag{14}$$

The above dispersion function, which is derived from Eqs. (3) and (7), differs slightly from that obtained by a rigorous treatment of $\mathbf{v}_{\perp}$-dependence of $\tilde{f}$ as mentioned after Eq. (7), although the difference is small for low perpendicular wave numbers $b_{\mathbf{k}}<1$.

The closure relation given by Eqs. (12) and (13) is derived from the assumption that the relation should be valid for a complex-conjugate pair of the linear kinetic eigenfunctions $f_{L\mathbf{k}}(v_{\parallel})$ and $f_{L\mathbf{k}}^*(v_{\parallel})$ as well as for any linear combination of them [see Eqs. (23)–(29) in Ref. 14]. Existence of this pair reflects the time reversal symmetry of the collisionless kinetic equation, and one of the eigenfunctions corresponds to a growing solution when the other corresponds to a decaying one. In conventional linear problems, only the dominant growing solution is considered while its conjugate partner is usually disregarded. However, in the three-mode ITG problem, which is the simplest example of nonlinear

kinetic systems, transitions between growing and decaying phases occur repeatedly and the nonlinear solution is given by the superposition of $f_{L\mathbf{k}}(v_\parallel)$ and $f^*_{L\mathbf{k}}(v_\parallel)$ so that the NCM is successfully applied.[14] Numerical simulations in the next section reveal that the basic idea of the NCM mentioned above also works for a better description of the anomalous transport in the strong ITG turbulence.

Before showing simulation results, it is meaningful to consider kinetic and fluid entropy balances in the slab ITG turbulence based on the governing equations in the same manner as in Ref. 14. We define the microscopic entropy S_m and the macroscopic entropy S_M for ions per unit volume by[22,23] $S_m=-\int dv_\parallel f \ln f$ and $S_M=-\int dv_\parallel F_M \ln F_M$, where $f=F_M+\tilde{f}$. [Here, both f and $\tilde{f}$ are regarded as distribution functions on the $v_\parallel$-space obtained by integrating those in Eqs. (1) and (2) on the $\mathbf{v}_\perp$-space so that $\tilde{f}=\Sigma_{\mathbf{k}} f_{\mathbf{k}}(v_\parallel,t)e^{i\mathbf{k}\cdot\mathbf{x}}$.] Retaining terms up to $\mathcal{O}(\tilde{f}^2)$, the relation between S_m and S_M is given by $S_M=\langle S_m\rangle+\frac{1}{2}\int dv_\parallel\langle\tilde{f}^2\rangle/F_M$, where $(\cdots)$ represents the ensemble average. As shown from Eq. (1), the total microscopic entropy $\int d^3x S_m$ is conserved without collisions, although the macroscopic entropy S_M or $\Delta S\equiv\frac{1}{2}\int dv_\parallel\langle\tilde{f}^2\rangle/F_M$ can increase through the turbulent or anomalous transport processes. [Krommes and Hu[24] called $\overline{\mathcal{S}}\equiv-\frac{1}{2}\int dv_\parallel\langle\tilde{f}^2\rangle/F_M (=S_m-S_M$ in our notation) the entropy of the system to measure deviation of the fluctuating distribution function $\tilde{f}$ from the ensemble-averaged distribution function $\langle f\rangle$ although we here regard $\Delta S=S_M-S_m (=-\overline{\mathcal{S}}=\overline{\mathcal{F}}$ in Krommes and Hu[24]) as the entropy associated with the fluctuations because, in the collisionless system, turbulent processes produce not S_m but S_M.] Throughout the present work, we consider the system in the uniform magnetic field, and assume the turbulent fluctuations to be statistically homogeneous in space. (Such homogeneous turbulence is actually obtained by simulations in the next section.) Then, we replace the ensemble average $\langle\cdots\rangle$ by the volume average such that $\Delta S\equiv\frac{1}{2}\int dv_\parallel\langle\tilde{f}^2\rangle/F_M=\frac{1}{2}\Sigma_{\mathbf{k}}\int dv_\parallel|f_{\mathbf{k}}|^2/F_M$.

From Eqs. (3), (7), and (9), we find that the turbulent entropy production rate is given by

$$\frac{d}{dt}\left(\sum_{\mathbf{k}}\int dv_\parallel\frac{|f_{\mathbf{k}}|^2}{2F_M}\right)=n_0\sum_{\mathbf{k}}\left[\mathrm{Re}\left(\frac{T^*_{\mathbf{k}}}{2T_i}\frac{ic}{B}\mathbf{b}\times\mathbf{k}\Psi_{\mathbf{k}}\right)\cdot(-\nabla\ln T_i)+\frac{e\ \mathrm{Re}(-ik_\parallel\Psi_{\mathbf{k}}u^*_{\mathbf{k}})}{T_i}\right]=\frac{\mathbf{q}_\perp}{T_i}\cdot(-\nabla\ln T_i)+\frac{Q}{T_i},\tag{15}$$

where $\mathbf{q}_\perp\equiv\frac{1}{2}n_0\Sigma_{\mathbf{k}}\mathrm{Re}[T^*_{\mathbf{k}}i(c/B)\mathbf{b}\times\mathbf{k}\Psi_{\mathbf{k}}]$ is the turbulent perpendicular ion heat flux and $Q\equiv en_0\Sigma_{\mathbf{k}}\mathrm{Re}(-ik_\parallel\Psi_{\mathbf{k}}u^*_{\mathbf{k}})$ represents the turbulent ion heating. Using Eqs. (4), (7), and (9), we obtain

$$\frac{d}{dt}\left(\sum_{\mathbf{k}}\frac{n_0}{2}\left|\frac{e\phi_{\mathbf{k}}}{T_e}\right|^2\left[1+\frac{T_e}{T_i}\{1-\Gamma_0(b_{\mathbf{k}})\}\right]\right)=-\frac{Q}{T_e}.\tag{16}$$

Then, using Eq. (16), the kinetic entropy balance equation (15) is rewritten as

$$\frac{d}{dt}\sum_{\mathbf{k}}\left(\int dv_\parallel\frac{|f_{\mathbf{k}}|^2}{2F_M}+\frac{n_0T_e}{2T_i}\left|\frac{e\phi_{\mathbf{k}}}{T_e}\right|^2\left[1+\frac{T_e}{T_i}\{1-\Gamma_0(b_{\mathbf{k}})\}\right]\right)=\frac{\mathbf{q}_\perp}{T_i}\cdot(-\nabla\ln T_i).\tag{17}$$

It is convenient to expand $f_{\mathbf{k}}$ in terms of the Hermite polynomials $H_n(x)\equiv(-1)^n e^{x^2/2}d^ne^{-x^2/2}/dx^n$ $(x\equiv v_\parallel/v_t;\ n=0,1,2,\ldots)$ as

$$\begin{aligned}f_{\mathbf{k}}(v_\parallel,t)&=F_M(v_\parallel)\sum_n\varphi_{n\mathbf{k}}(t)H_n(v_\parallel/v_t)\\&=F_M(v_\parallel)\left[\frac{n_{\mathbf{k}}}{n_0}+\frac{u_{\mathbf{k}}}{v_t}\left(\frac{v_\parallel}{v_t}\right)+\frac{1}{2}\frac{T_{\mathbf{k}}}{T_i}\left\{\left(\frac{v_\parallel}{v_t}\right)^2-1\right\}\right.\\&\quad+\frac{1}{6}\frac{q_{\mathbf{k}}}{n_0T_iv_t}\left\{\left(\frac{v_\parallel}{v_t}\right)^3-3\left(\frac{v_\parallel}{v_t}\right)\right\}\\&\quad\left.+\sum_{n\geqslant4}\varphi_{n\mathbf{k}}(t)H_n(v_\parallel/v_t)\right],\end{aligned}\tag{18}$$

where $\varphi_{n\mathbf{k}}(t)=(n!)^{-1}\int_{-\infty}^{\infty}d(v_\parallel/v_t)f_{\mathbf{k}}(v_\parallel,t)H_n(v_\parallel/v_t)$ $(n=0,1,2,\ldots)$. Substituting Eq. (18) into Eq. (17) gives

$$\begin{aligned}&\frac{d}{dt}\sum_{\mathbf{k}}n_0\left(\frac{1}{2}\left|\frac{n_{\mathbf{k}}}{n_0}\right|^2+\frac{1}{2}\left|\frac{u_{\mathbf{k}}}{v_t}\right|^2+\frac{1}{4}\left|\frac{T_{\mathbf{k}}}{T_i}\right|^2+\frac{1}{12}\left|\frac{q_{\mathbf{k}}}{n_0T_iv_t}\right|^2\right.\\&\quad\left.+\sum_{n\geqslant4}\frac{n!}{2}|\varphi_{n\mathbf{k}}|^2+\frac{T_e}{2T_i}\left|\frac{e\phi_{\mathbf{k}}}{T_e}\right|^2\left[1+\frac{T_e}{T_i}\{1-\Gamma_0(b_{\mathbf{k}})\}\right]\right)\\&\quad=\frac{\mathbf{q}_\perp}{T_i}\cdot(-\nabla\ln T_i),\end{aligned}\tag{19}$$

where the orthogonality conditions for the Hermite polynomials $(2\pi)^{-1/2}\int_{-\infty}^{\infty}dx\ e^{-x^2/2}H_n(x)H_m(x)=n!\,\delta_{nm}$ $(n,m=0,1,2,\ldots)$ are used. It is found from Eq. (17) or Eq. (19) that there is no perpendicular heat transport in the direction of the temperature gradient in the collisionless steady turbulent state where saturation of the entropy $\int dv_\parallel|f_{\mathbf{k}}|^2/2F_M$ and the potential amplitude $|\phi_{\mathbf{k}}|$ occurs. Then, we assume a *quasisteady* state[14] in which the amplitudes of the fluid variables $\varphi_{n\mathbf{k}}$ with low n ($n_{\mathbf{k}}$, $u_{\mathbf{k}}$, $T_{\mathbf{k}}$, $q_{\mathbf{k}}$, ...) and the potential $\phi_{\mathbf{k}}$ reach the steady state while the high-n moments included in $\Sigma_{n\geqslant4}(n!/2)|\varphi_{n\mathbf{k}}|^2$ grow indefinitely in time. (The quasisteady state should be regarded as idealization of the real steady state in which those high-n moments eventually saturate as well due to collisional dissipation even if the collision frequency is much smaller than the characteristic frequency of the instabilities causing the turbulence.)

Using Eqs. (4)–(7) and (10), we can derive another balance equation similar to Eq. (19),

$$\frac{d}{dt}\sum_{\mathbf{k}} n_0\left(\frac{1}{2}\left|\frac{n_{\mathbf{k}}}{n_0}\right|^2+\frac{1}{2}\left|\frac{u_{\mathbf{k}}}{v_t}\right|^2+\frac{1}{4}\left|\frac{T_{\mathbf{k}}}{T_i}\right|^2 + \frac{T_e}{2T_i}\left|\frac{e\phi_{\mathbf{k}}}{T_e}\right|^2\left[1+\frac{T_e}{T_i}\{1-\Gamma_0(b_{\mathbf{k}})\}\right]\right) = \frac{\mathbf{q}_\perp}{T_i}\cdot(-\nabla\ \ln T_i)+\sum_{\mathbf{k}}\ \mathrm{Re}\left(\frac{T_{\mathbf{k}}}{2T_i^2}ik_\parallel q_{\mathbf{k}}^*\right), \tag{20}$$

which can be regarded as the fluid entropy balance equation. We should note that Eq. (20) is valid irrespectively of closure relations. Comparing Eq. (20) to Eq. (19), we easily find

$$\sum_{\mathbf{k}}\ \mathrm{Re}\left(\frac{T_{\mathbf{k}}}{2T_i^2}ik_\parallel q_{\mathbf{k}}^*\right) = -\frac{d}{dt}\sum_{\mathbf{k}}\ n_0\left(\frac{1}{12}\left|\frac{q_{\mathbf{k}}}{n_0T_iv_t}\right|^2 + \sum_{n\geqslant 4}\frac{n!}{2}|\varphi_{n\mathbf{k}}|^2\right). \tag{21}$$

For the quasisteady state in which $d(\Sigma_{n\leqslant 3}(n!/2)\,|\varphi_{n\mathbf{k}}|^2)/dt=0$, we obtain from Eqs. (20) and (21),

$$\frac{\mathbf{q}_\perp}{T_i}\cdot(-\nabla\ \ln T_i) = -\sum_{\mathbf{k}}\ \mathrm{Re}\left(\frac{T_{\mathbf{k}}}{2T_i^2}ik_\parallel q_{\mathbf{k}}^*\right) = \frac{d}{dt}\left(n_0\sum_{\mathbf{k}}\sum_{n\geqslant 4}\frac{n!}{2}|\varphi_{n\mathbf{k}}|^2\right). \tag{22}$$

Equation (22) represents the entropy production rate in the quasisteady state, where the perpendicular heat transport in the presence of the background temperature gradient drives the growth of the fluctuations in the high-n moment variables through the correlation between the parallel heat flux and temperature fluctuations. It is interesting to note that, in a closed fluid system, the correlation term $\mathrm{Re}[(T_{\mathbf{k}}/2T_i^2)ik_\parallel q_{\mathbf{k}}^*]$ involved in the entropy balance is influenced by what closure model is used. The entropy balance equations in Eqs. (17) and (20) are also useful for checking numerical accuracy of nonlinear simulations of the collisionless slab ITG turbulence.

III. SIMULATION RESULTS

Here, results of kinetic and fluid simulations of the two-dimensional slab ITG turbulence are shown. We consider a rectangular domain of $L_x\times L_y$ in the x–y plane with a uniform external magnetic field $\mathbf{B}=B(\hat{\mathbf{z}}+\theta\hat{\mathbf{y}})$ ($|\theta|\ll 1$), where $\hat{\mathbf{y}}$ and $\hat{\mathbf{z}}$ denote the unit vectors in the y- and z-directions, respectively. The system is assumed to be homogeneous in the z-direction ($\partial/\partial z=0$). We employ the periodic boundary conditions in both x and y directions. Then, in Eq. (2), we can write $\mathbf{k}=k_x\hat{\mathbf{z}}+k_y\hat{\mathbf{y}}=2\pi[(m/L_x)\hat{\mathbf{x}}+(n/L_y)\hat{\mathbf{y}}]$, $f_{\mathbf{k}}=f_{m,n}$, and $\phi_{\mathbf{k}}=\phi_{m,n}$ ($m,n=0,\pm 1,\pm 2,\ldots$) and the parallel wave number is given by $k_\parallel=k_y\theta$. The background density and temperature gradients are assumed to exist in the x-direction, and their gradient scale lengths are given by $L_n=-(d\ \ln n_0/dx)^{-1}(>0)$ and $L_T=-(d\ \ln T_i/dx)^{-1}(>0)$, respectively.

The governing equations for the kinetic simulation are written in Eqs. (3) and (7) for $k_\parallel\neq 0$ and Eq. (9) for $k_\parallel=0$.

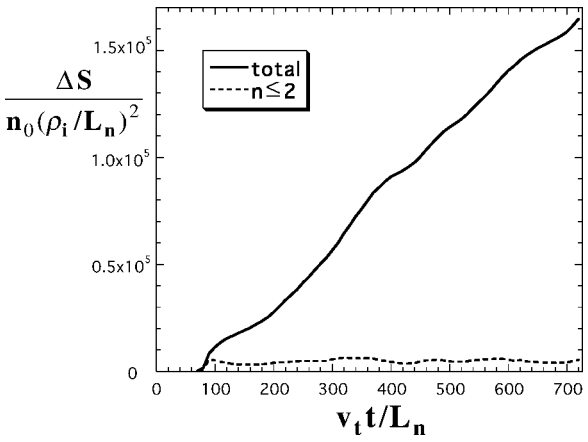

FIG. 1. Time evolution of the entropy associated with the fluctuations per unit volume $\Delta S\equiv\frac{1}{2}\int dv_\parallel\langle\tilde{f}^2\rangle/F_M$ obtained by the kinetic simulation. Solid and dotted lines correspond to ΔS and $\Delta S^{(n\leqslant 2)}\equiv n_0\Sigma_{\mathbf{k}}(\frac{1}{2}|n_{\mathbf{k}}/n_0|^2+\frac{1}{2}|u_{\mathbf{k}}/v_t|^2+\frac{1}{4}|T_{\mathbf{k}}/T_i|^2)$, respectively.

For comparison to the kinetic simulation, two types of fluid simulations using different closure models are done. Both fluid simulations are based on Eqs. (4)–(7) for $k_\parallel\neq 0$ and Eq. (10) for $k_\parallel=0$. However, one of them employs the NCM given by Eq. (12) for linearly unstable modes and the HP dissipative closure given by Eq. (11) for linearly stable modes while the other uses the HP closure for all modes. Here, for all simulations, we use the conditions $T_e/T_i=1$, $\eta_i=L_n/L_T=10$, and $L_x=L_y=20\pi\rho_i$ [$\rho_i\equiv v_t/\Omega_i$ is the ion thermal gyroradius]. Another important parameter related to the linear dispersion relation is $\Theta\equiv\theta L_n/\rho_i$. We find from Eq. (14) that the normalized complex-valued eigenfrequency $\omega_{L\mathbf{k}}/\omega_{*i}$ is a function of the dimensionless parameters $(k_\perp\rho_t,\Theta,\eta_i,T_e/T_i)$. Simulation results for $\Theta=2$ are shown in Figs. 1–8.

Figure 1 shows time evolution of the entropy associated with the fluctuations per unit volume $\Delta S\equiv\frac{1}{2}\int dv_\parallel\langle\tilde{f}^2\rangle/F_M$, which is obtained by the kinetic simulation. Here, solid and dotted lines correspond to ΔS and $\Delta S^{(n\leqslant 2)}$, respectively, where $\Delta S^{(n\leqslant 2)}\equiv n_0\Sigma_{\mathbf{k}}(\frac{1}{2}|n_{\mathbf{k}}/n_0|^2+\frac{1}{2}|u_{\mathbf{k}}/v_t|^2+\frac{1}{4}|T_{\mathbf{k}}/T_i|^2)$ represents a contribution from the $n\leqslant 2$ terms in the Hermite-polynomial expansion of $f_{\mathbf{k}}$ to ΔS [see Eq. (18)]. It is clearly seen that, even after the end of the linear stage at $v_tt/L_n\simeq 90$, ΔS continues to monotonically increase while $\Delta S^{(n\leqslant 2)}$ is saturated. This implies realization of the quasisteady state of the collisionless turbulence described in the previous section, which was already confirmed by Watanabe and Sugama.[19] The monotonic increase of ΔS is sustained by generation of fine velocity-space structures of $f_{\mathbf{k}}$ through phase-mixing processes such as the ballistic mode. In order to keep enough resolution for the fine structures, 8193 grid points are used here for discretization of the velocity space, $-5\leqslant v_\parallel/v_t\leqslant 5$. Also, in order to satisfy the kinetic entropy balance equation in Eq. (17) with high accuracy, we employ the time integrator, which retain the time reversal symmetry and avoid numerical dissipation.[25] The kinetic computation

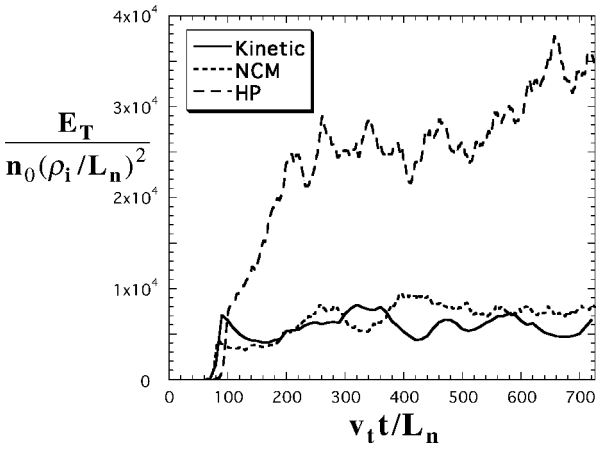

FIG. 2. Time evolution of $E_T \equiv \Sigma_{\mathbf{k}} n_0(\frac{1}{2}|n_{\mathbf{k}}/n_0|^2+\frac{1}{2}|u_{\mathbf{k}}/v_t|^2+\frac{1}{4}|T_{\mathbf{k}}/T_i|^2 + \frac{1}{2}(T_e/T_i)|e\phi_{\mathbf{k}}/T_e|^2[1+(T_e/T_i)\{1-\Gamma_0(b_{\mathbf{k}})\}])$. Solid, dotted, and dashed curves represent results of the kinetic, NCM, and HP simulations, respectively.

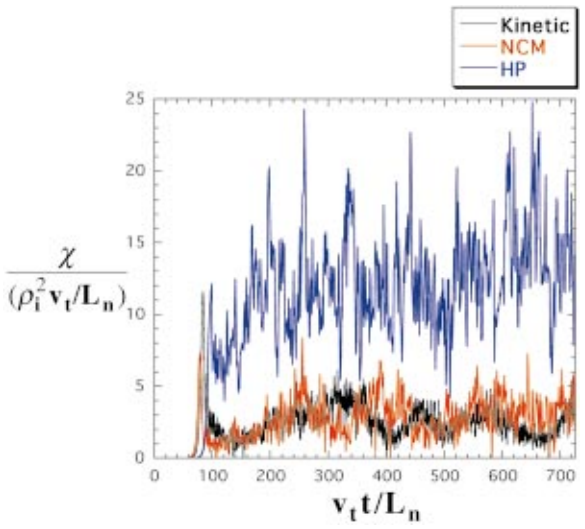

FIG. 3. (Color) Normalized perpendicular heat diffusivity $\chi/(\rho_i^2 v_t/L_n)$ as a function of normalized time $v_t t/L_n$. Black, red, and blue lines correspond to results of the kinetic, NCM, and HP simulations, respectively.

should be stopped when the velocity-space scale of the ballistic mode reaches the grid size (at $v_t t/L_n > 800$ for the present case).

For all kinetic and fluid simulations, we impose the same initial condition that the initial amplitude $(e\phi_{\mathbf{k}}/T_e)/(\rho_i/L_n) = 10^{-5}$ and random phases are given to all potential components $\phi_{\mathbf{k}}$ with $k_\parallel \neq 0$. The mode wave numbers used here are $(k_x,k_y) = 0.1\rho_i^{-1}(m,n)$ with $m,n = 0,\pm 1,\pm 2,\ldots,\pm 32$, for which good numerical convergence is obtained. It is confirmed that, in the early time stage, the kinetic simulation, the NCM fluid simulation, and the one using only the HP closure model show a good agreement on the growth of the linear unstable modes because both the NCM and the HP model accurately reproduce the kinetic linear dispersion relation. Figure 2 shows time evolution of the energy-like quantity,

$$E_T \equiv \sum_{\mathbf{k}} n_0 \left(\frac{1}{2}\left|\frac{n_{\mathbf{k}}}{n_0}\right|^2 + \frac{1}{2}\left|\frac{u_{\mathbf{k}}}{v_t}\right|^2 + \frac{1}{4}\left|\frac{T_{\mathbf{k}}}{T_i}\right|^2 + \frac{T_e}{2T_i}\left|\frac{e\phi_{\mathbf{k}}}{T_e}\right|^2 \left[1 + \frac{T_e}{T_i}\{1-\Gamma_0(b_{\mathbf{k}})\} \right] \right), \tag{23}$$

the change rate of which is governed by Eq. (20). In Fig. 2, results of the kinetic, NCM, and HP simulations are represented by solid, dotted, and dashed curves, respectively. We find from Fig. 2 that the nonlinear saturation label of E_T in the HP simulation is much larger than that in the kinetic simulation while the NCM simulation result is closer to the kinetic one.

Figure 3 shows the normalized perpendicular heat diffusivity $\chi/(\rho_i^2 v_t/L_n)$ as a function of normalized time $v_t t/L_n$, where $\chi \equiv \mathbf{q}_\perp \cdot \hat{\mathbf{x}}/(n_0 T_i/L_T)$ and $\mathbf{q}_\perp \equiv \frac{1}{2} n_0 \Sigma_{\mathbf{k}} \mathrm{Re}[T_{\mathbf{k}}^* i(c/B)\mathbf{b} \times \mathbf{k}\Psi_{\mathbf{k}}]$. Here, black, red, and blue lines correspond to results of the kinetic, NCM, and HP simulations, respectively. We see that χ shows similar behaviors to those of E_T in Fig. 2 except that more spiky oscillations appear in the former. In the saturated state of turbulence, χ obtained by the NCM simulation is in good agreement with χ from the kinetic simulation. In contrast, χ obtained by the HP simulation are significantly larger than them. We obtain $(\overline{\chi},\Delta\chi)/(\rho_i^2 v_t/L_n) = (2.57,0.97)$, $(3.06,1.30)$, and $(12.86,3.43)$ from the kinetic, NCM, and HP simulations, respectively, where $\overline{\chi}$ and $\Delta\chi$ denote the time average and the standard deviation of χ over $300 \leqslant v_t t/L_n \leqslant 726$, respectively. The NCM simulation also reproduces a big fall of χ after the first overshoot shown by the kinetic one better than the HP simulation.

Patterns of the electrostatic potential on the (x,y)-plane at $v_t t/L_n = 726$ obtained by the kinetic, NCM, and HP simulations are shown in Figs. 4(a), 4(b), and 4(c), respectively. For all cases, more isotropic vortex structures are seen in the nonlinear stage than in the linear stage where the structure of the $(m,n) = (0,4)$ [or $(k_x\rho_i, k_y\rho_i) = (0.1m, 0.1n) = (0,0.4)$] mode with the largest linear growth rate is dominant. We notice that the HP simulation gives the largest amplitude of the potential.

In order to investigate in more detail the difference between the turbulent heat diffusivities shown in Fig. 3, we plot $\overline{\chi_{\mathbf{k}}}$ for linearly unstable modes with $(k_x\rho_i, k_y\rho_i) = (0,0.1),\ldots,(0,0.7)$ in Fig. 5, where $\overline{\chi_{\mathbf{k}}}$ is defined by taking a time average of the wave-number-dependent heat diffusivity $\chi_{\mathbf{k}} \equiv \mathbf{q}_{\perp\mathbf{k}} \cdot \hat{\mathbf{x}}/(n_0 T_i/L_T) \equiv -\frac{1}{2}\mathrm{Re}[T_{\mathbf{k}}^* i(c/B)k_y \Psi_{\mathbf{k}}]/(T_i/L_T)$ over $300 \leqslant v_t t/L_n \leqslant 726$. Here, black, red, and blue lines correspond to the kinetic, NCM, and HP simulation results, respectively. It is noted that $\overline{\chi_{\mathbf{k}}}$'s for other unstable modes with $k_x \neq 0$, which are not shown here, tend to become smaller with increasing k_x. In Fig. 5, the normalized linear growth rates $\gamma_{\mathbf{k}}/(v_t/L_n)$ are also plotted by thin dashed and dotted curves, which correspond to results from the NCM and the HP model, respectively. [For unstable modes, the linear growth rates obtained by the kinetic model coincide with those by the NCM because of definitions of the real-valued closure coefficients in Eq. (13).] Due to the inverse cascade, contributions to χ are dominantly made by lower

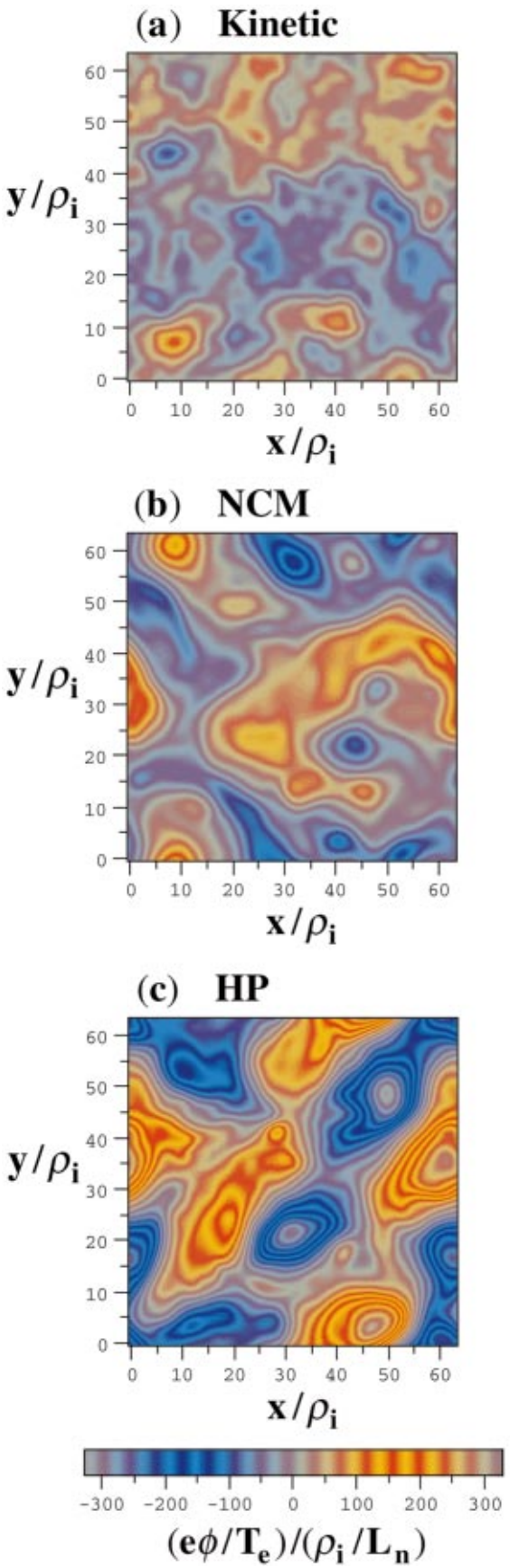

FIG. 4. (Color) Patterns of the electrostatic potential on the (x,y)-plane at $v_t t/L_n = 726$ obtained by (a) kinetic, (b) NCM, and (c) HP simulations.

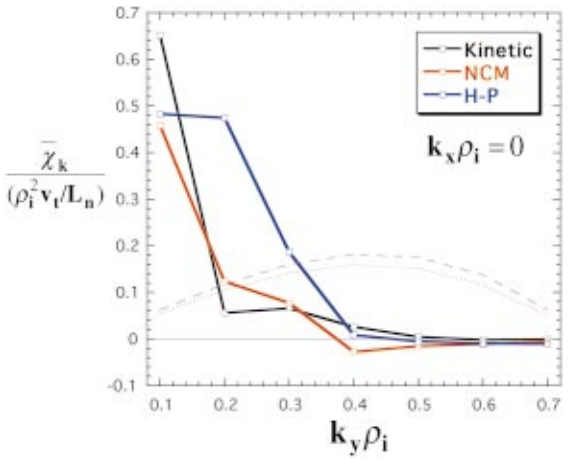

FIG. 5. (Color) Contributions of linearly unstable modes with $(k_x\rho_i, k_y\rho_i) = (0,0.1), \ldots, (0,0.7)$ to the turbulent heat diffusivity. Symbols on black, red, and blue lines represent $\overline{\chi_{\mathbf{k}}}/(\rho_i^2 v_t/L_n)$ obtained by the kinetic, NCM, and HP simulations, respectively. Here, $\overline{\chi_{\mathbf{k}}}$ is defined by taking a time average of $\chi_{\mathbf{k}} \equiv \mathbf{q}_{\perp\mathbf{k}} \cdot \hat{\mathbf{x}}/(n_0 T_i/L_T) \equiv -\frac{1}{2}\mathrm{Re}[T_{\mathbf{k}}^* i(c/B)k_y \Psi_{\mathbf{k}}]/(T_i/L_T)$ over $300 \leqslant v_t t/L_n \leqslant 726$. The normalized linear growth rates $\gamma_{\mathbf{k}}/(v_t/L_n)$ calculated from the NCM and the HP model are also plotted by thin dashed and dotted curves, respectively. (For unstable modes, the linear growth rates obtained by the kinetic model coincide with those by the NCM.)

wave number modes than the most unstable $(k_x\rho_i, k_y\rho_i) = (0,0.4)$ mode. We find that, in the kinetic and NCM simulations, the lowest wave number $(k_x\rho_i, k_y\rho_i) = (0,0.1)$ mode plays a dominant role in the turbulent heat transport while, in the HP simulation, other low wave number modes such as the $(k_x\rho_i, k_y\rho_i) = (0,0.2)$ and $(0,0.3)$ modes also give relatively large contributions to χ, which leads to significantly larger χ in the HP simulation as seen in Fig. 3.

Figures 6(a) and 6(b) show the wave-number-dependent heat diffusivity $\chi_{\mathbf{k}}$ as a function of time for the cases of $(k_x\rho_i, k_y\rho_i) = (0,0.1)$ and $(0,0.2)$, respectively. Here, black, red, and blue curves correspond to the kinetic, NCM, and HP simulation results, respectively. As seen from Fig. 6(a), all kinetic, NCM, and HP simulations show similar behaviors of $\chi_{\mathbf{k}}$ for the lowest wave number unstable mode $(k_x\rho_i, k_y\rho_i) = (0,0.1)$ in the nonlinearly saturated state: Average values and distribution widths of $\chi_{\mathbf{k}}$ in the three simulations are close to one another. On the other hand, we find from Fig. 6(b) that, for $(k_x\rho_i, k_y\rho_i) = (0,0.2)$, $\chi_{\mathbf{k}}$'s distributions in the kinetic and NCM simulations become much smaller than for $(k_x\rho_i, k_y\rho_i) = (0,0.1)$ while $\chi_{\mathbf{k}}$'s behaviors in the HP simulation for the two cases of $(k_x\rho_i, k_y\rho_i) = (0,0.1)$ and $(0,0.2)$ are not much different from each other. It should be especially noted that, in the kinetic and NCM simulations for $(k_x\rho_i, k_y\rho_i) = (0,0.2)$, there appears a significant length of time for $\chi_{\mathbf{k}}$ to be negative, which is a contrast to the case of $(k_x\rho_i, k_y\rho_i) = (0,0.1)$.

Now, let us consider how the results shown above are related to the closure relations. We directly check the validity of the closure relations themselves for the parallel heat flux $q_{\mathbf{k}}$ by examining what values the ratio of $q_{\mathbf{k}}$ to the temperature fluctuation $T_{\mathbf{k}}$ takes in the kinetic and fluid simulations. The real and imaginary parts of $q_{\mathbf{k}}/(n_0 v_t T_{\mathbf{k}})$ are plotted as a function of time in Fig. 7. Figures 7(a) and 7(b) show

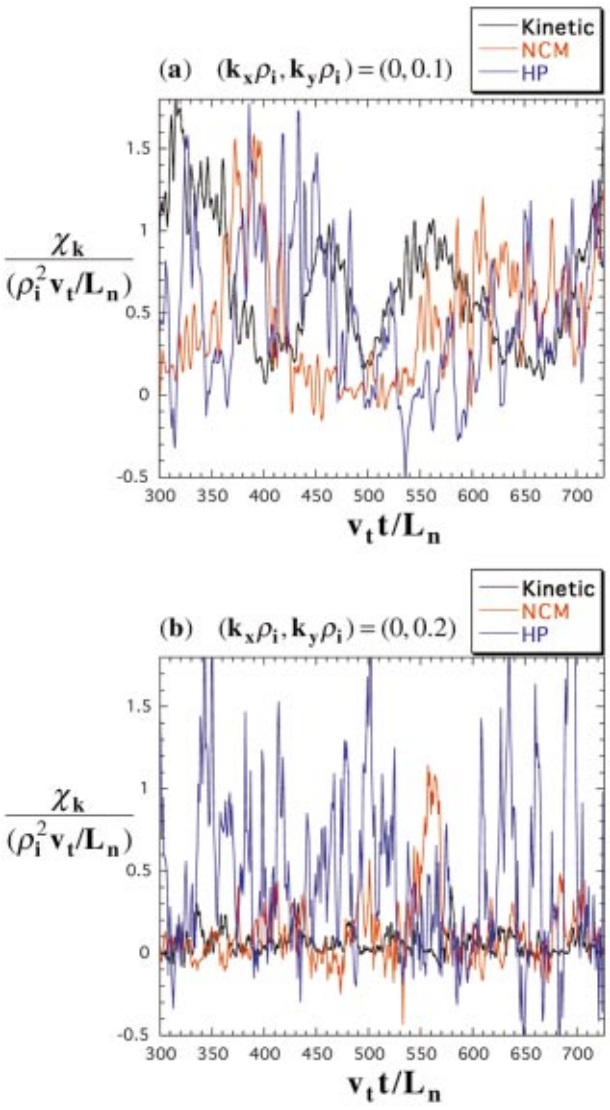

FIG. 6. (Color) The wave-number-dependent heat diffusivity $\chi_{\mathbf{k}}$ as a function of time for the cases of (a) $(k_x\rho_i, k_y\rho_i)=(0,0.1)$ and (b) $(k_x\rho_i, k_y\rho_i)=(0,0.2)$. Here, black, red, and blue curves correspond to the kinetic, NCM, and HP simulation results, respectively.

$\mathrm{Re}[q_{\mathbf{k}}/(n_0 v_t T_{\mathbf{k}})]$ and $\mathrm{Im}[q_{\mathbf{k}}/(n_0 v_t T_{\mathbf{k}})]$ for the lowest wave number unstable mode $(k_x\rho_i\, k_y\rho_i)=(0,0.1)$, respectively, while their correspondences for the case of $(k_x\rho_i, k_y\rho_i)=(0,0.2)$ are given in Figs. 7(c) and 7(d). Here, results from the kinetic and NCM simulations are represented by black and red curves, respectively. In the HP model, $\mathrm{Re}[q_{\mathbf{k}}/(n_0 v_t T_{\mathbf{k}})]=0$ and $\mathrm{Im}[q_{\mathbf{k}}/(n_0 v_t T_{\mathbf{k}})]=-2(2/\pi)^{1/2}\simeq -1.5958$ as shown by blue horizontal lines. It is found from the kinetic result that both real and imaginary parts of $q_{\mathbf{k}}/(n_0 v_t T_{\mathbf{k}})$ are oscillatory functions of time, which is better described by the NCM than by the HP. The oscillation amplitudes of the real and imaginary parts in the kinetic simulation are about the same as those in the NCM simulation, and these amplitudes become smaller for the lower wave number mode. Up to the early part of the nonlinear stage $[v_t t/L_n<200$ for $(k_x\rho_i\, k_y\rho_i)=(0,0.1)$ and $v_t t/L_n<150$ for $(k_x\rho_i\, k_y\rho_i)=(0,0.2)]$, the kinetic and NCM results show a good agreement on the behaviors of $\mathrm{Re}[q_{\mathbf{k}}/(n_0 v_t T_{\mathbf{k}})]$ and $\mathrm{Im}[q_{\mathbf{k}}/(n_0 v_t T_{\mathbf{k}})]$ although, in the later time, the values of both real and imaginary part in the NCM case slightly shift in the positive direction on average from those in the kinetic case.

The sign of $\mathrm{Im}[q_{\mathbf{k}}/(n_0 v_t T_{\mathbf{k}})]$ is especially important since it determines the sign of the dissipation term $\mathrm{Re}[\frac{1}{2}(T_{\mathbf{k}}/T_i^2) i k_\parallel q_{\mathbf{k}}^*]$ in the entropy balance [see Eq. (20)]. For $k_\parallel>0$, negative (positive) $\mathrm{Im}[q_{\mathbf{k}}/(n_0 v_t T_{\mathbf{k}})]$ corresponds to dissipation (antidissipation) and to positive (negative) $\chi_{\mathbf{k}}$ if we assume that the mode structure is given by or close to a linear combination of the unstable linear eigenfunctions and its complex conjugates. [This assumption is valid for the three-mode ITG problem[14] and is supported to some extent for the collisionless turbulence as shown in Watanabe and Sugama,[19] where it is checked by the kinetic simulation how closely $f_{\mathbf{k}}(v_\parallel)$ for the linearly most unstable mode takes the form of $c_1 f_{L\mathbf{k}}(v_\parallel)+c_2 f_{L\mathbf{k}}^*(v_\parallel)$ with the linear eigenfunction $f_{L\mathbf{k}}(v_\parallel)$ and its complex conjugate $f_{L\mathbf{k}}^*(v_\parallel)$.] The kinetic and NCM results in Fig. 7(b) show that, for the lowest wave number unstable mode $(k_x\rho_i\, k_y\rho_i)=(0,0.1)$, $\mathrm{Im}[q_{\mathbf{k}}/(n_0 v_t T_{\mathbf{k}})]$ is almost always negative as in the HP model, which means that the mode structure for $(k_x\rho_i\, k_y\rho_i)=(0,0.1)$ stays close to that of the unstable eigenfunction. This fact is related to the large positive χ values for $(k_x\rho_i\, k_y\rho_i)=(0,0.1)$ shown in Figs. 5 and 6(a). On the other hand, for $(k_x\rho_i\, k_y\rho_i)=(0,0.2)$, the kinetic and NCM simulations show that the length of time for $\mathrm{Im}[q_{\mathbf{k}}/(n_0 v_t T_{\mathbf{k}})]$ to be positive increases as seen in Fig. 7(d). Then, the $(k_x\rho_i\, k_y\rho_i)=(0,0.2)$ mode structure can sometimes approach the complex conjugate of the unstable eigenfunction, which enables $\chi_{\mathbf{k}}$ to reduce or take negative values as shown in Fig. 6(b). This fact is confirmed more clearly in Fig. 8, where $\chi_{\mathbf{k}}$ and $\mathrm{Im}[q_{\mathbf{k}}/(n_0 v_t T_{\mathbf{k}})]$ for $(k_x\rho_i\, k_y\rho_i)=(0,0.2)$ are plotted as a function of time on the same frame. Figures 8(a) and 8(b) correspond to the kinetic and NCM simulations, respectively. It is obvious that positive (negative) $\mathrm{Im}[q_{\mathbf{k}}/(n_0 v_t T_{\mathbf{k}})]$ correlates with negative (positive) $\chi_{\mathbf{k}}$. Allowing for this positive $\mathrm{Im}[q_{\mathbf{k}}/(n_0 v_t T_{\mathbf{k}})]$ in the NCM is considered to be the key to the better prediction of χ than in the HP model.

Figure 9 shows the normalized perpendicular heat diffusivity $\chi/(\rho_i^2 v_t/L_n)$ as a function of normalized time $v_t t/L_n$ for the case of $\Theta=1$. Parameters used here are the same as in Figs. 1–8 except for Θ. The linear growth rate of the most unstable mode increases from $\gamma_{\max}=0.182(v_t/L_n)$ at $(k_x\rho_i, k_y\rho_i)=(0,0.4)$ for $\Theta=2$ to $\gamma_{\max}=0.379(v_t/L_n)$ at $(k_x\rho_i, k_y\rho_i)=(0,0.7)$ for $\Theta=1$. Also, the wave number region for unstable modes extends from $k_\perp\rho_i\leqslant 0.7$ for $\Theta=2$ to $k_\perp\rho_i\leqslant 1.2$ for $\Theta=1$. Thus, the heat diffusivity χ in the nonlinearly saturated state becomes larger for $\Theta=1$ than for $\Theta=2$. Still, the NCM simulation describes the behavior of χ in the kinetic simulation better than the HP model because of the same reason as explained in the case of $\Theta=2$.

IV. CONCLUSIONS

In the present paper, we have made a detailed comparison between kinetic and fluid simulations of two-dimensional collisionless slab ITG turbulence. In the fluid simulations, two types of different closure relations, namely,

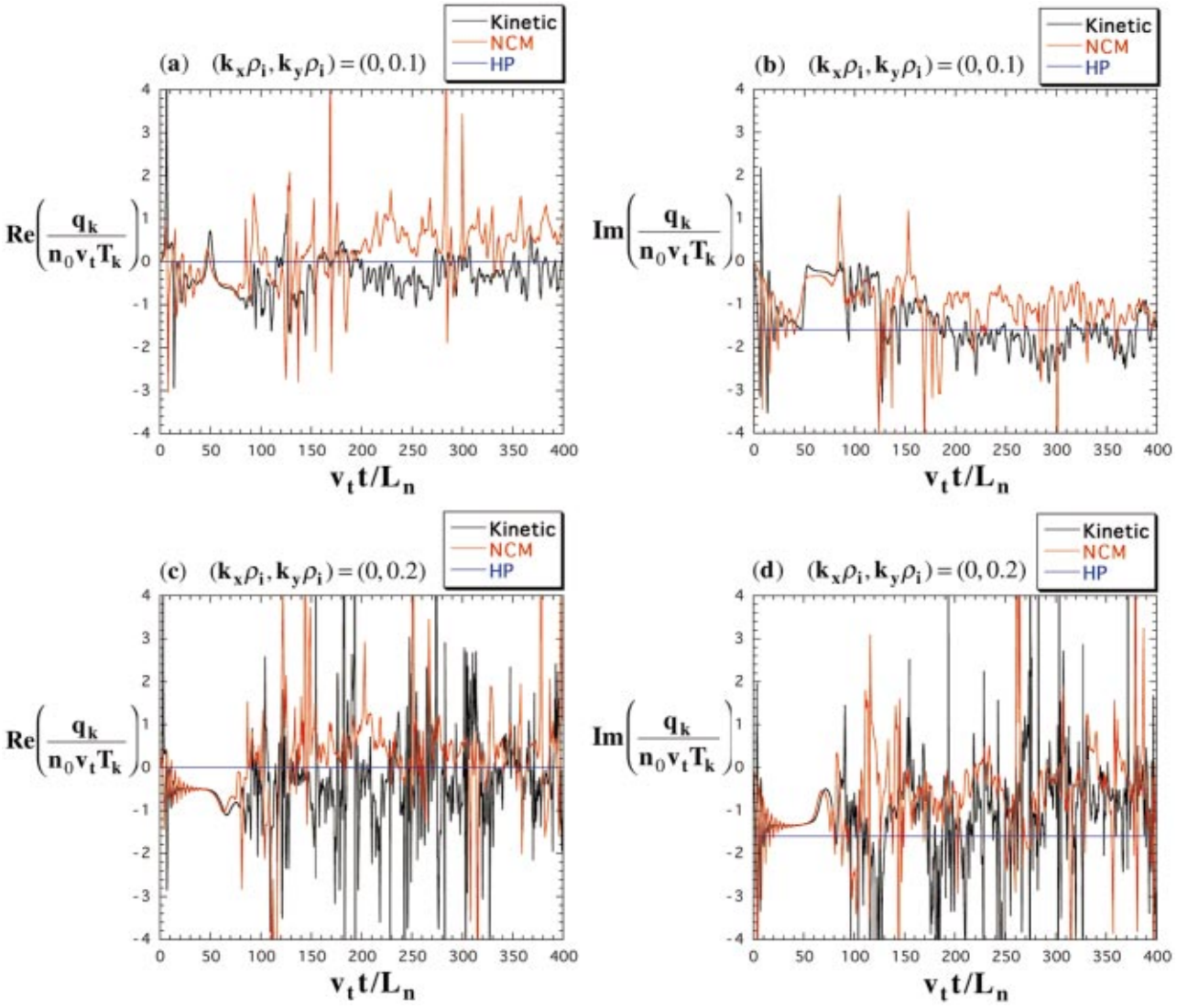

FIG. 7. (Color) Real and imaginary parts of $q_{\mathbf{k}}/(n_0 v_t T_{\mathbf{k}})$ as a function of normalized time $v_t t/L_n$. Here, $\mathrm{Re}[q_{\mathbf{k}}/(n_0 v_t T_{\mathbf{k}})]$ and $\mathrm{Im}[q_{\mathbf{k}}/(n_0 v_t T_{\mathbf{k}})]$ for the lowest wave number unstable mode $(k_x\rho_i\, k_y\rho_i) = (0,0.1)$ are shown in (a) and (b), respectively, while their correspondences for the case of $(k_x\rho_i, k_y\rho_i) = (0,0.2)$ are given in (c) and (d). Results from the kinetic and NCM simulations are represented by black and red curves, respectively. Blue horizontal lines correspond to the HP model, in which $\mathrm{Re}[q_{\mathbf{k}}/(n_0 v_t T_{\mathbf{k}})] = 0$ and $\mathrm{Im}[q_{\mathbf{k}}/(n_0 v_t T_{\mathbf{k}})] = -2(2/\pi)^{1/2} \simeq -1.5958$.

the NCM and the HP model are employed for linearly unstable modes. We examine how accurately they can reproduce nonlinear results of the kinetic simulation such as the turbulent heat diffusivity χ. In the collisionless kinetic simulation with no zonal flow component, the quasisteady turbulent state is reached, in which the entropy variable associated with fine velocity-space structures $\Delta S \equiv \frac{1}{2}\int dv_\parallel \langle \tilde{f}^2 \rangle / F_M$ monotonically increases while the low-n fluid variables and the electrostatic potential reach the real steady state. (Here, n denotes the number of order in the Hermite polynomial expansion of the distribution function.)

We show that the saturation level of the low-n fluid variables and χ in the quasisteady state of the kinetic simulation are better predicted by the fluid simulation using the NCM than by the one using the HP model. In the kinetic and NCM simulations, unstable modes other than the lowest-wave-number unstable mode have low amplitudes and small contributions to the turbulent heat transport while, in the HP simulation, the number of unstable modes with significant effects on the transport increases, which leads to the higher saturation value of χ. The kinetic and fluid simulation results all show that the contribution of the lowest-wave-number unstable mode to the turbulent diffusivity χ always tends to take relatively large positive values, which is associated with the dissipative nature of the relation between the parallel heat flux $q_{\mathbf{k}}$ and the temperature fluctuation $T_{\mathbf{k}}$ that the imaginary part of the ratio $q_{\mathbf{k}}/T_{\mathbf{k}}$ for that mode is constantly negative. However, it is a common property found in the kinetic and NCM simulations that, for other low-wave-number unstable modes, $\chi_{\mathbf{k}}$ can take negative values in response to $\mathrm{Im}(q_{\mathbf{k}}/T_{\mathbf{k}})$ becoming positive. The HP model misses this mechanism and causes χ to be larger. Here, $\chi_{\mathbf{k}}$ represents the contribution of the mode with the wave number vector $\mathbf{k}$ to the total heat diffusivity χ, and the meaning of negative $\chi_{\mathbf{k}}$ is that the $\mathbf{E}\times\mathbf{B}$ convective thermal flux produced by that mode is up the background temperature gradient.

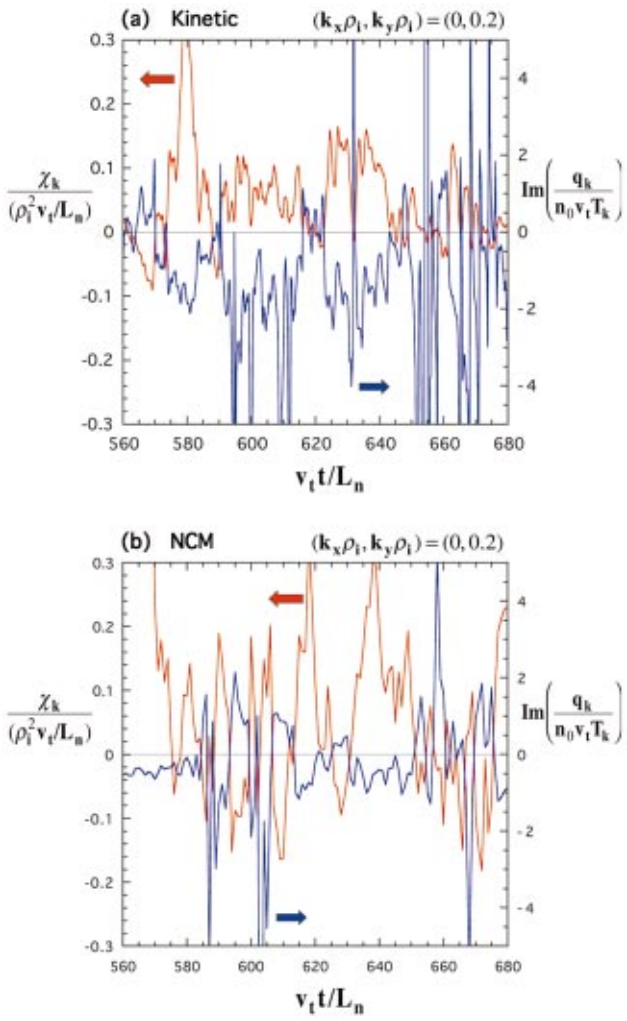

FIG. 8. (Color) Time evolution of $\chi/(\rho_i^2 v_t/L_n)$ and $\mathrm{Im}[q_{\mathbf{k}}/(n_0 v_t T_{\mathbf{k}})]$ for $(k_x\rho_i\, k_y\rho_i)=(0,0.2)$. Results from the kinetic and NCM simulations are shown in (a) and (b), respectively. Red and blue curves represent $\chi/(\rho_i^2 v_t/L_n)$ and $\mathrm{Im}[q_{\mathbf{k}}/(n_0 v_t T_{\mathbf{k}})]$, respectively.

The real and imaginary parts of the ratio $q_{\mathbf{k}}/T_{\mathbf{k}}$ for unstable modes obtained by the NCM simulation are oscillatory functions of time, which have distribution widths similar to those in the kinetic case, although the averaged values in the former shift from those in the latter in the positive direction. So, there is still room for improvement of the NCM to reproduce the kinetic results more accurately. Also, extensions of the present work to the cases including important effects such as toroidal geometries, zonal flows, and electromagnetic fluctuations remain as future problems.

Finally, based on the results obtained in the present work, we remark our views on an adequate fluid closure for the plasma with zonal flows. There, a proper treatment of zonal flow components is important as shown in Ref. 18. In addition, we expect that the nondissipative nature of unstable modes still needs to be described by the closure. Especially in such a case as in the low-confinement mode, the zonal flow effects are relatively weak and many unstable modes exist so that an accurate treatment of them is crucial to evaluation of the turbulent transport coefficient. On the other hand, when zonal flows are dominant, turbulence suppression can be treated by either dissipative or nondissipative closure. However, the zonal flows and the unstable modes often show pulsation behavior through their interaction[18] and both play a important role in the plasma transport. Thus, generally the use of the nondissipative closure for the unstable modes is considered preferable although some modification of the closure relation may be necessary in order to take account of the variation of the unstable mode structures due to the zonal flows.

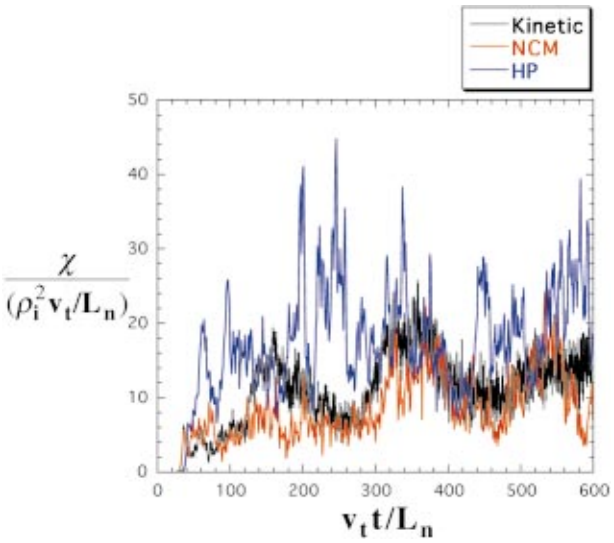

FIG. 9. (Color) Normalized perpendicular heat diffusivity $\chi/(\rho_i^2 v_t/L_n)$ as a function of normalized time $v_t t/L_n$. Black, red, and blue lines correspond to results of the kinetic, NCM, and HP simulations, respectively. Parameters used here are the same as in Figs. 1–8 except for $\Theta=1$.

ACKNOWLEDGMENTS

Numerical computations of the kinetic and fluid equations are performed on the NIFS MISSION System (Man-Machine Interactive System for Simulation) and the NIFS General Purpose Computer System, respectively. This work is supported in part by the Japanese Ministry of Education, Culture, Sports, Science, and Technology, Grant Nos. 12680497 and 14780387, the U.S. Department of Energy, Grant No. DE-FG03-96ER-54346, and the National Science Foundation, Grant No. ATM-9907673.

[1] A. M. Dimits, G. Bateman, M. A. Beer *et al.*, Phys. Plasmas **7**, 969 (2000).
[2] W. Horton, Rev. Mod. Phys. **71**, 735 (1999).
[3] W. Dorland and G. W. Hammett, Phys. Fluids B **5**, 812 (1993).
[4] R. E. Waltz, G. D. Kerbel, and J. Milovich, Phys. Plasmas **1**, 2229 (1994).
[5] M. A. Beer, G. W. Hammett, G. Rewoldt, E. J. Synakowski, M. C. Zarnstorff, and W. Dorland, Phys. Plasmas **4**, 1792 (1997).
[6] W. W. Lee and W. M. Tang, Phys. Fluids **31**, 612 (1988).
[7] S. E. Parker, W. W. Lee, and R. A. Santoro, Phys. Rev. Lett. **71**, 2042 (1993).
[8] A. M. Dimits, T. J. Williams, J. A. Byers, and B. I. Cohen, Phys. Rev. Lett. **77**, 71 (1996).
[9] Z. Lin, T. S. Hahm, W. W. Lee, W. M. Tang, and R. B. White, Science **281**, 1835 (1998).
[10] G. W. Hammett and F. W. Perkins, Phys. Rev. Lett. **64**, 3019 (1990).
[11] Z. Chang and J. D. Callen, Phys. Fluids B **4**, 1167 (1992).
[12] N. Mattor and S. E. Parker, Phys. Rev. Lett. **79**, 3419 (1997).

[13]S. E. Parker, W. Dorland, R. A. Santoro, M. A. Beer, Q. P. Liu, W. W. Lee, and G. W. Hammett, Phys. Plasmas **1**, 1461 (1994).
[14]H. Sugama, T.-H. Watanabe, and W. Horton, Phys. Plasmas **8**, 2617 (2001).
[15]T.-H. Watanabe, H. Sugama, and T. Sato, Phys. Plasmas **7**, 984 (2000).
[16]P. W. Terry, Rev. Mod. Phys. **72**, 109 (2000).
[17]M. N. Rosenbluth and F. L. Hinton, Phys. Rev. Lett. **80**, 724 (1998).
[18]M. A. Beer and G. W. Hammett, in *Proceedings of the Joint Varenna-Lausanne International Workshop on Theory of Fusion Plasmas, Varenna, 1998*, edited by J. W. Connor, E. Sindoni, and J. Vaclavik (Societa Italiana di Fisica, Bologna, Italy, 1999), p. 19.
[19]T.-H. Watanabe and H. Sugama, Phys. Plasmas **9**, 3659 (2002).
[20]Z. Lin, T. S. Hahm, W. W. Lee, W. M. Tang, and R. B. White, Phys. Plasmas **7**, 1857 (2000).
[21]D. H. E. Dubin, J. A. Krommes, C. Oberman, and W. W. Lee, Phys. Fluids **26**, 3524 (1983).
[22]H. Sugama and W. Horton, Phys. Plasmas **2**, 2989 (1995).
[23]H. Sugama, M. Okamoto, W. Horton, and M. Wakatani, Phys. Plasmas **3**, 2379 (1996).
[24]J. A. Krommes and G. Hu, Phys. Plasmas **1**, 3211 (1994).
[25]T.-H. Watanabe, H. Sugama, and T. Sato, J. Phys. Soc. Jpn. **70**, 3565 (2001).